Date Paper

How to Cite: *J. Inorg. Mater.*, 2026, **41(10):** 1517
DOI: 10.15541/jim20260021

Density Functional Theory Computation of Mo-adsorbed Two-dimensional Boron-nitrogen Monolayers for Nitrogen Reduction Reaction

LI Zhi[1], ZHANG Junmiao[1], FENG Ziyang[1], XIAO Beibei[1], SONG Erhong[2]

(1. School of Energy and Power Engineering, Jiangsu University of Science and Technology, Zhenjiang 212003, China; 2. Shanghai Institute of Ceramics, Chinese Academy of Sciences, Shanghai 200050, China)

Abstract: Electrocatalytic nitrogen reduction reaction (NRR) is regarded as a promising route for sustainable ammonia synthesis, but developing highly active and selective catalysts remains a critical challenge. In this work, the density functional theory calculations were performed to investigate the NRR performance of Mo-adsorbed B_2N, B_3N and B_4N monolayers. The strong interaction between Mo and its substrate ensures the good stability, as reflected by the binding energies of –8.39, –5.91 and –6.75 eV for Mo-adsorbed B_2N, B_3N and B_4N monolayers, respectively. The adsorbed Mo sites are able to activate the N_2 molecule, elongating the N≡N bond length from 1.108 Å in the gas phase to 1.128, 1.132 and 1.132 Å on Mo-B_2N, Mo-B_3N and Mo-B_4N, respectively. Free energy profile analysis reveals that the thermodynamic barriers are 1.21, 1.07 and 0.61 eV for Mo-B_2N, Mo-B_3N and Mo-B_4N, with Mo-B_4N exhibiting the highest activity. This trend clearly demonstrates that the Mo reactivity is well-tuned by its coordination. Furthermore, the electronic structure analysis shows a relation between the strength of N≡N bond and the thermodynamic energy, where a weaker strength of N≡N bond indicates a better NRR activity. Mo-B_4N material also exhibits a high thermodynamic stability, as reflected by the robustness of the structural rigidity wherein no structural collapse is observed under the room temperature of 300 K. Therefore, Mo-B_4N is expected to be an active and durable catalyst for the NRR. This study provides theoretical guidance for the design of NRR electrocatalysts and proposes viable candidate systems for experimental synthesis. The datasets in this article are listed in Science Data Bank at https://www.doi.org/10.57760/sciencedb.jim.00043.

Key words: nitrogen reduction reaction; density functional theory; single-atom catalysis

Carbon neutrality, the equilibrium between carbon emissions and removal, has garnered global consensus due to the imminent threat of climate change. Shifting from high-energy consuming technologies to sustainable, fossil-free alternatives for producing globally significant chemicals renders a crucial contribution to effectively reducing carbon dioxide emissions. As is well known, ammonia is a pivotal chemical with widespread applications[1-3]. Industrially, ammonia is massively produced by Haber-Bosch process[4-5], which requires substantial energy input to split the strong N≡N bond (941 kJ/mol)[6], leading to large CO_2 emissions. Alternatively, electrochemistry can effectively drive the nitrogen reduction reaction (NRR) under ambient temperature and pressure. However, its efficiency is heavily dependent on the availability of suitable catalytic materials[7]. Hence, it is imperative to develop an active and durable catalytic material for the application of N_2-to-NH_3 conversion.

Ru is known to be active toward N_2 activation and protonation, but such noble metal-based catalysts suffer from limited resources and high cost. Therefore, the development of transition metal-based catalysts is urgently needed. Specifically, single-atom catalysts (SACs) have been numerically investigated owing to their distinct advantages, including well-defined active sites and maximized atom utilization[8-9]. For example, Chen *et al.*[10] revealed a good NRR activity of Mo

Received date: 2026-01-14; **Revised date:** 2026-04-10; **Published online:** 2026-04-16
Biography: LI Zhi (2000–), male, Master candidate. E-mail: 19708893695@163.com
李 智(2000–), 男, 硕士研究生. E-mail: 19708893695@163.com
Corresponding author: ZHANG Junmiao, lecturer. E-mail: zjmin2001@just.edu.cn; SONG Erhong, associate professor. E-mail: ehsong@mail.sic.ac.cn
张俊苗, 讲师. E-mail: zjmin2001@just.edu.cn; 宋二红, 副研究员. E-mail: ehsong@mail.sic.ac.cn

anchored on BC_2N. Zhao *et al*.[11] found the low energy barrier to be 0.66 eV when catalyzed by $Mo_3(HAB)_2$ monolayer. Shi *et al*.[12] determined a thermodynamic energy barrier of 0.43 eV for Mo-doped graphdiyne. Furthermore, Xu *et al*.[13] identified Mo-doped C_4N_3 as a promising candidate with an overpotential of 0.76 V. Liang *et al*.[14] reported an overpotential of 0.41 V for Mo@C_3N_3. Wang *et al*.[15] found that MoPc-TFPN exhibited an ultralow overpotential of 0.21 V. Based on the information, two-dimensional materials with Mo decoration have attracted interest for electrocatalytic ammonia synthesis. Moreover, the catalytic activity of Mo is significantly influenced by its substrate, underscoring the critical importance of selecting a suitable substrate.

As reported, B_2N, B_3N and B_4N show different atomic structures[16]. The basic building blocks for B_2N are pentagons composed of two N atoms and three B atoms and an octagon ring with two embedded N atoms. B_3N has a more complex configuration where triangles, pentagons and two types of hexagons coexist. B_4N has the same triangles and hexagons of B_3N, which can be considered as two hexagonal chains separated by one triangle chain. These structures endow them with distinguished physical and chemical properties that could be used in varied applications. For instance, Rahimi *et al*.[17] demonstrated the gas detection performance offered by B_2N toward hazardous gases. Sredojević *et al*.[18] reported a good CO_2 reduction reaction (CO_2RR) activity delivered by V doped B_3N. Wei *et al*.[19] investigated the hydrogen adsorption properties of Na-decorated B_4N. Therefore, it is of great significance to explore whether B_2N, B_3N and B_4N could be used as the support of Mo atom in the NRR application.

To address this issue, the NRR performance of Mo-adsorbed B_2N, B_3N and B_4N monolayers was systematically investigated using density functional theory calculations. Firstly, the thermodynamically stable configurations were confirmed based on binding energy. Then, the adsorption configuration of N_2 molecule was determined. Finally, the free energy profiles of NRR *via* distal, alternative and enzymatic pathways were fully evaluated. The results demonstrate that Mo-B_4N exhibits the best activity with a limiting potential of 0.61 V. This work provides a theoretical understanding of the activity tuned by the different substrates.

1 Computational method

In this work, all simulations were conducted within the framework of density functional theory (DFT) as implemented in the DMol^3 software package[20-21]. The exchange-correlation interactions were described by the generalized gradient approximation (GGA) employing the Perdew-Burke-Ernzerhof (PBE) function[22]. A selection of GGA-PBE functional is well adopted in relevant computational studies[22-23]. A double numerical atomic orbital basis set augmented with polarization functions (DNP) was adopted to expand the electronic wave functions[24]. To facilitate stable electronic convergence, a thermal smearing of 0.005 Ha (1 Ha= 27.2114 eV) was applied to the orbital occupancy. The Brillouin zone integration was performed using a *k*-point sampling of 1×1×1. Structural relaxations were performed with convergence tolerances of 1.0×10^{-5} Ha for energy, 0.002 Ha/Å for maximum force, and 0.005 Å for maximum displacement. No strategy of van der Waals correction is adopted owing to the negligible influence of adsorption energies, as demonstrated in Table S1 (supporting materials). Spin polarization was considered throughout all calculations. For the atomic models, the periodic slab models were constructed to represent the substrates by using (1×3), (1×2), and (1×4) supercells for B_2N, B_3N, and B_4N structures, respectively. A vacuum layer of 25 Å was introduced along the *z*-direction to eliminate spurious interactions between periodic images. Furthermore, the finite-temperature stability of the systems was evaluated *via ab initio* molecular dynamics (AIMD) simulations at 300 K. These simulations were conducted within the canonical ensemble (NVT) using the Massive GGM thermostat to control the temperature, with a total simulation time of 10 ps and a timestep of 1 fs. According to the previous work[25], to reduce the calculational cost, the substrates were fully constrained during the frequency calculations required for thermodynamic corrections.

Detailed calculation formulas are shown in supporting materials.

2 Results and discussion

Fig. 1(a) shows the atomic structures of B_2N, B_3N and B_4N with Mo decoration. Mo is introduced into the two-dimensional substrate as the active site due to its activity reported previously[10-15, 26]. To evaluate the stability of Mo decoration, the binding energy E_b between Mo and its substrate was calculated. E_b are −8.39, −5.91 and −6.75 eV for Mo-B_2N, Mo-B_3N and Mo-B_4N, respectively. Furthermore, the d electron distribution is significantly modulated by the different substrates, with d-band center ε_d values of −2.28, −1.64 and −2.03 eV for Mo-B_2N, Mo-B_3N and Mo-B_4N,

respectively. The stronger E_b corresponds to the lower d-band center[27], as evidenced by linear fitting presented in Fig. 1(b). As reported, there is an inverse relationship between stability and reactivity in single atom catalysis[28], and the active atom endowed with stronger interaction with its substrate would deliver weaker adsorption ability. Therefore, it is reasonable to expect varied catalytic activity arising from the different d band electron distributions. The charge density difference (CDD) plots are shown in Fig. 1(c), providing the visualization of the interaction between the Mo atom and the substrate. To further reveal its underlying origin, the partial density of states (PDOS) of Mo d-band and B/N p-band were analyzed, as presented in Fig. 1(d). Clear p-d orbital coupling is observed below the Fermi level for Mo-B_2N, Mo-B_3N and Mo-B_4N, demonstrating the formation of covalent bonds, which is consistent with the strong E_b.

Subsequently, N_2 adsorption and activation were investigated[29]. Fig. 2(a) presents the N_2 adsorption configurations *via* side-on and end-on manners. For N_2 adsorption on Mo-B_2N, only end-on manner is observed with a free energy change of nitrogen adsorption $\Delta G_{ads}(N_2)$ of −0.67 eV. For Mo-B_3N, $\Delta G_{ads}(N_2)$ are −0.81 and −1.78 eV for side-on and end-on manners, respectively. For Mo-B_4N, they are −0.57 and −0.74 eV, respectively. Thus, the end-on manner is thermodynamically preferred for Mo-B_2N, Mo-B_3N and Mo-B_4N. The free energy changes of hydrogen adsorption ΔG_H were evaluated, which are −0.57, −0.17 and −0.33 eV for Mo-B_2N, Mo-B_3N and Mo-B_4N, respectively. As previously reported, Wu *et al*.[30] found that the Ru-N_4 catalyst exhibited stronger N_2 adsorption than H adsorption, thereby promoting the NRR. Similarly, Gao *et al*.[31] reported that various single-metal atom catalysts supported on phosphotungstic acid (PTA) also demonstrated stronger N_2 adsorption over H adsorption, significantly inhibiting the hydrogen evolution reaction (HER). Thus, stronger N_2 adsorption compared to H adsorption is advantageous for HER suppression. In this work, all systems exhibit preferential adsorption of N_2 over H, which would be beneficial for suppressing the HER. The ΔG_H is dependent on the applied potential U, and the preferential adsorption of N_2 over H cannot be maintained when U increases to 0.10 V for Mo-adsorbed B_2N, 1.61 V for Mo-adsorbed B_3N and 0.41 V for Mo-adsorbed B_4N, respectively (Fig. S1). Therefore, the complete suppression of HER is impossible, which is commonly observed experimentally due to its short reaction pathway and fast kinetics[32].

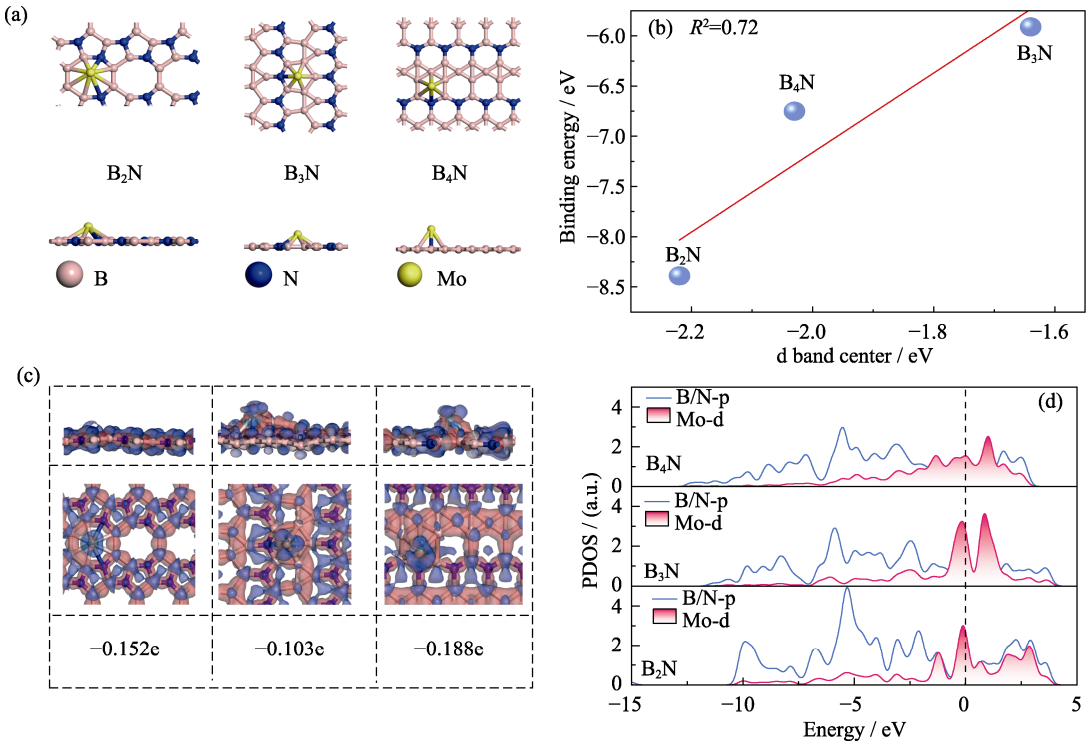


Fig. 1 (a) Model structures; (b) Linear relationship between d-band center and binding energy; (c) Iso-surface plots of the charge density difference (CDD) and charge transfer quantities; (d) Partial density of states (PDOS) analysis for Mo interacting with B_2N, B_3N and B_4N substrates, respectively, with the p-band contributions from B_2N, B_3N and B_4N represented the combined p-bands of B and N atoms directly bonded to metal atoms in each structure

To characterize the activation of adsorbed N_2 (*N_2), Fig. 2(b) presents PDOS between Mo d-band and *N_2 p-band. The favorable alignment between Mo d-orbitals and N_2 p-orbitals promotes significant p-d orbital hybridization, which facilitates N_2 activation. Furthermore, the electronic density of states at the Fermi level facilitates efficient electron transfer, thereby weakening the N≡N bond. CDD plots presented in Fig. 2(c) illustrate the clear electronic interactions between the Mo atom and *N_2 molecules in Mo-B_4N. Mulliken charges of *N_2 are −0.026e, −0.123e and −0.117e when adsorbed on Mo-B_2N, Mo-B_3N and Mo-B_4N, respectively. In this regard, electrons are transferred from the catalysts to the *N_2 adsorbate, leading to the elongation of N≡N bond from 1.108 Å of free nitrogen molecule to 1.128, 1.132 and 1.132 Å of the *N_2 adsorbate upon adsorption on Mo-B_2N, Mo-B_3N and Mo-B_4N, respectively. To quantitatively evaluate bond strength of N≡N bond, crystal orbital Hamilton population (COHP) was analyzed. As shown in Fig. 2(d), the integrated COHP (–ICOHP) values decrease dramatically from 15.12 for free N_2 to 5.25, 4.63 and 4.35 for the *N_2 adsorbate upon adsorption on Mo-B_2N, Mo-B_3N and Mo-B_4N, respectively. Therefore, the weakened bond strength confirms effective N_2 activation, which facilitates subsequent protonation steps.

Subsequently, the NRR activity was evaluated *via* thermodynamic analysis. Figs. 3(a-c) present the free energy profiles of Mo-B_4N along the distal, alternating and enzymatic pathways, respectively. For the distal pathway, the free energy changes ΔG of the protonation steps are 0.61, −0.04, −0.01, −0.74, −0.51 and 0.13 eV, respectively. The potential determining step (PDS) is the first protonation step, with a maximum thermodynamic barrier ΔG_{max} of 0.61 eV. For the alternating pathway, the ΔG values of the protonation steps are 0.61, 0.63, −0.88, 0.82, −2.35 and 0.61 eV, respectively. Herein, the PDS is located at *H_2NNH_2 formation, with a ΔG_{max} of 0.82 eV. For the enzymatic pathway, the corresponding ΔG values are 0.98, −0.07, −0.63, −1.33, −0.34 and 0.66 eV, respectively. The PDS is identified as the *NNH formation, with a ΔG_{max} of 0.98 eV. Therefore, the distal pathway is thermodynamically preferred for Mo-B_4N, with a required applied potential of 0.61 V. Following the same analysis, Table 1 summarizes the corresponding ΔG data. Similar to Mo-B_4N, the distal pathway is energetically favored for Mo-B_2N and Mo-B_3N, with the PDS of *NNH formation. However, ΔG_{max} increases to 1.21 and 1.07 eV, respectively. Fig. 3(d) presents the ΔG_{max} values of the Mo-B_2N, Mo-B_3N and Mo-B_4N, showing that Mo-B_4N outperforms Mo-B_2N and Mo-B_3N. Furthermore, compared to the benchmark Ru(001) catalyst, Mo-B_4N exhibits comparable performance for ammonia synthesis[33]. Besides, the ΔG_{max} data of this work and the previous works are summarized in Table S2[11-15, 26]. The activity

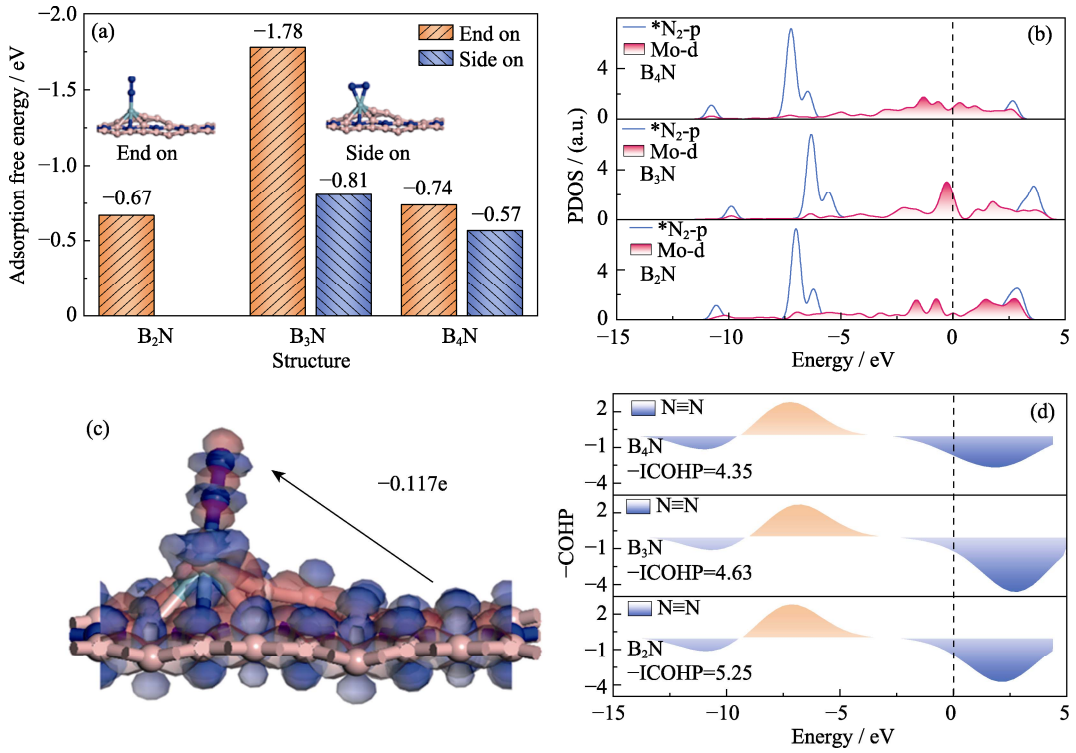


Fig. 2 (a) Adsorption free energies of N_2 under two adsorption configurations; (b) PDOS of Mo with N_2 adsorbate; (c) Charge transfer quantity for N_2 adsorbed on Mo-B_4N; (d) Crystal orbital Hamilton population (COHP) analysis of N≡N bond in adsorbed *N_2

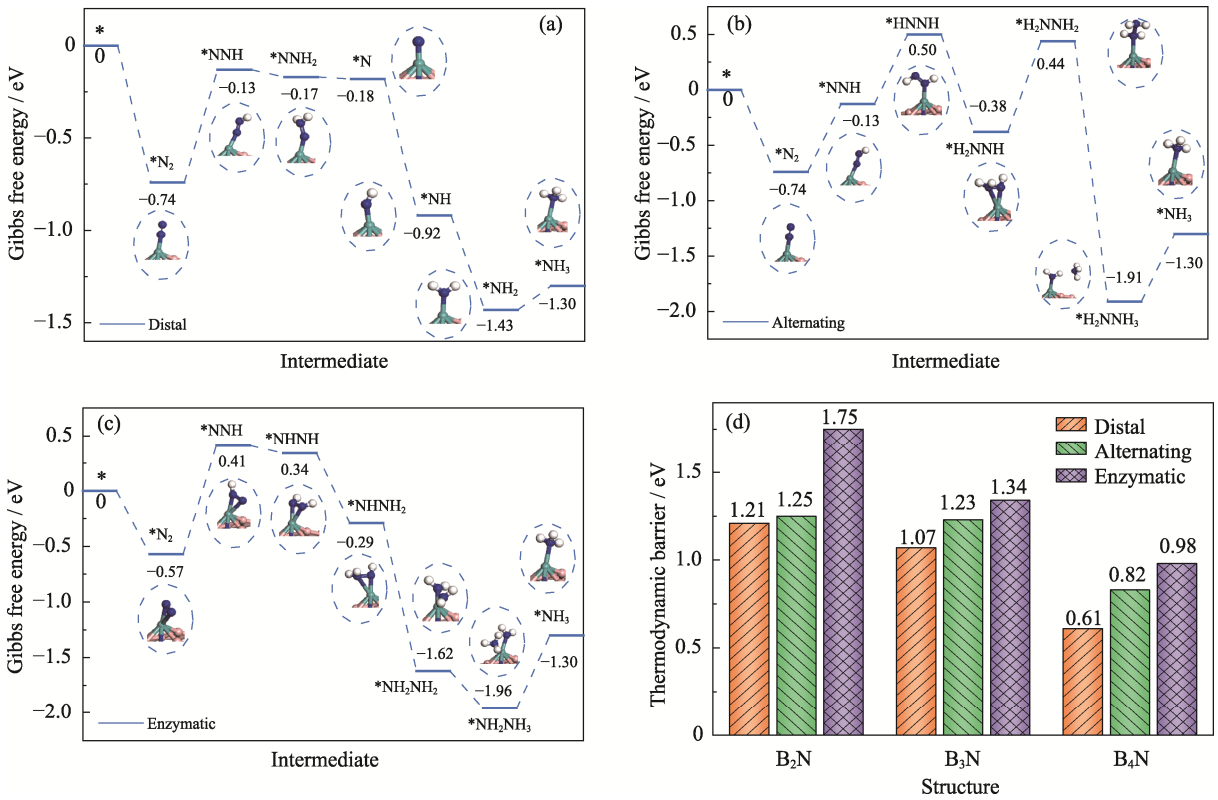


Fig. 3 (a) Distal pathway of Mo-B_4N; (b) Alternating pathway of Mo-B_4N; (c) Enzymatic pathway of Mo-B_4N; (d) Thermodynamic barriers of Mo-B_2N, Mo-B_3N and Mo-B_4N

of Mo single atoms varies significantly with the substrates, with corresponding ΔG_{max} ranging from 0.21 to 1.01 V. Herein, Mo-B_4N exhibits moderate activity compared to previous reports[11-15, 26].

To shed light on the underlying activity of Mo-B_4N, a detailed analysis focused on its electronic structure was performed. Fig. 4(a) presents the total density of states (TDOS) of Mo-B_4N with the adsorption of various N-containing intermediates. The electronic states are consistently presented at the Fermi level, indicating good metallic conductivity of Mo-B_4N, which facilitates electron transfer during protonation steps[34]. Furthermore, a linear relationship between the –ICOHP value and the thermodynamic barrier ΔG_{max} was established. As shown in Fig. 4(b), the superior activity of Mo-B_4N stems from its excellent N_2 activation capability. To further support its capability toward N_2 activation, the bond lengths of N–N ($d_{N–N}$) and Mo–N ($d_{Mo–N}$) were monitored during the protonation process. As shown in Fig. 4(c), the increased $d_{N–N}$ indicates a gradual weakening of the N–N bond, which is beneficial for its cleavage. After the cleavage of the N–N bond, the $d_{Mo–N}$ is gradually elongated during the last three protonation steps. A sharp increase in $d_{Mo–N}$ suggests a weakened interaction between the Mo site and the corresponding N-containing intermediates, which facilitates the recovery of Mo site. The desorption energy of NH_3 is 1.29 eV for Mo-B_4N. In previous works[35-43], the desorption energy of NH_3 falls within the range of 1.18 to 2.31 eV, revealing that the endothermic nature of NH_3 desorption is a universal phenomenon. With the aid of solution, the NH_3 desorption would not be an obstacle. Finally, the thermodynamic stability of Mo-B_4N at room temperature of 300 K was confirmed by AIMD calculations. Fig. 4(d) shows that despite energy fluctuations, Mo-B_4N maintains its structural integrity. According to the bond lengths between Mo and the surrounding B/N atoms as listed in Table 2 (different coordination atoms are labeled in Fig. S2), the changes of bond lengths are less than 0.240 Å, and all Mo–N and Mo–B bonds remain intact. Therefore, Mo-decorated B_4N is expected to be active and durable toward NRR. This theoretical work provides the potential candidate for the experimental synthesis.

3 Conclusions

In summary, this study systematically investigated the NRR performance of Mo-B_xN (x=2, 3, 4) monolayers using DFT calculations. The results indicate that the

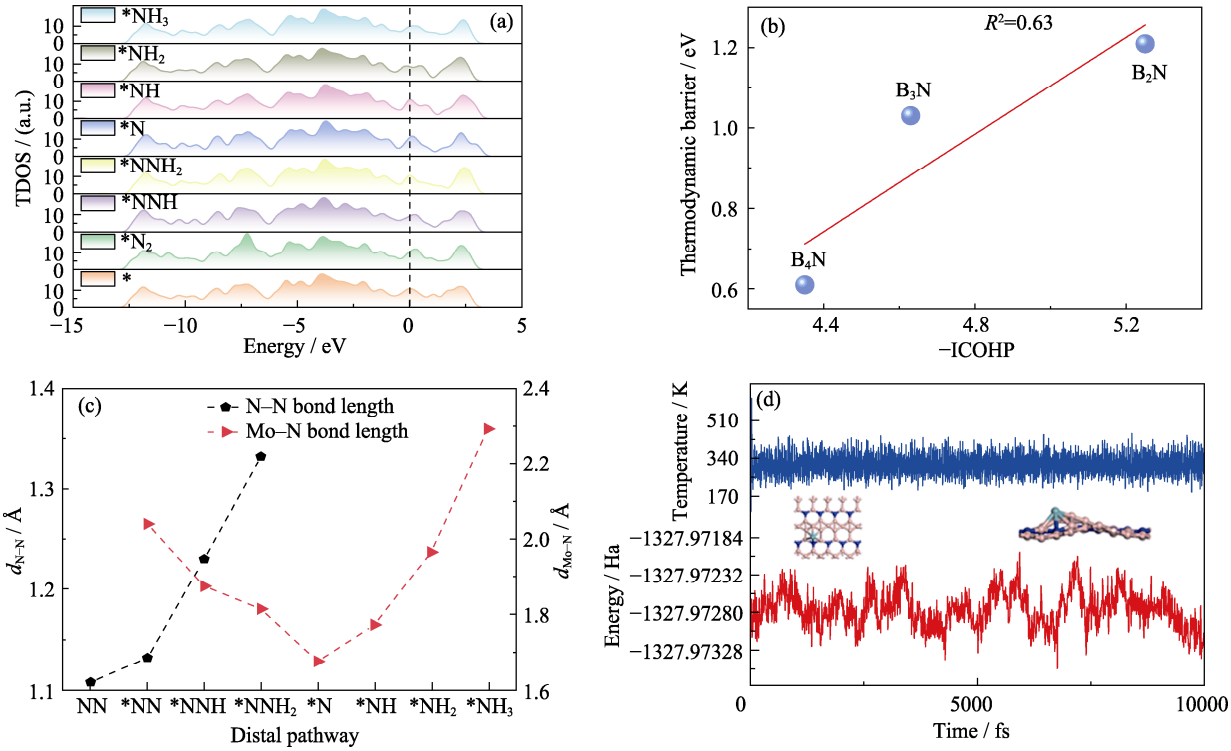


Fig. 4 (a) Total density of states (TDOS) of Mo-B_4N with varied N-containing intermediates along the distal pathway; (b) Linear relationship between –ICOHP of N≡N bond and thermodynamic energy barrier; (c) Bond lengths of N–N and Mo–N; (d) AIMD simulation of Mo-B_4N at room temperature of 300 K

Table 1 Free energy changes Δ*G* of elementary steps and thermodynamic barriers ΔG_{max}

Structure	Mechanism	ΔG/eV						ΔG$_{max}$/eV
Mo-B_2N	Distal	1.21	−0.32	−0.19	−0.44	−0.01	−0.90	1.21
	Alternating	1.21	0.08	−0.07	1.25	−2.29	−0.82	1.25
	Enzymatic	1.75	−0.43	−0.65	−0.67	−0.01	−0.50	1.75
Mo-B_3N	Distal	1.07	0.48	−0.76	−0.74	0.53	−0.12	1.07
	Alternating	1.07	1.23	−1.28	0.44	−1.71	0.70	1.23
	Enzymatic	0.64	−0.03	−0.65	−1.51	−0.32	1.34	1.34
Mo-B_4N	Distal	0.61	−0.04	−0.01	−0.74	−0.51	0.13	0.61
	Alternating	0.61	0.63	−0.88	0.82	−2.35	0.61	0.82
	Enzymatic	0.98	−0.07	−0.63	−1.33	−0.34	0.66	0.98

Table 2 Bond length between Mo and B/N atom

Time/ps		0	1	2	3	4	5	6	7	8	9	10
Bond length/Å	Mo–B1	2.325	2.270	2.210	2.258	2.368	2.321	2.317	2.342	2.198	2.298	2.242
	Mo–B2	2.209	2.141	2.174	2.211	2.194	2.215	2.267	2.148	2.161	2.162	2.325
	Mo–B3	2.249	2.245	2.209	2.317	2.148	2.277	2.239	2.204	2.261	2.181	2.257
	Mo–B4	2.029	2.048	2.030	2.023	2.017	2.048	2.006	2.043	2.069	2.004	2.091
	Mo–B5	2.081	2.087	2.178	2.179	2.111	2.053	2.082	2.084	2.188	2.089	2.102
	Mo–N	2.236	2.169	2.251	2.222	2.247	2.206	2.266	2.389	2.149	2.141	2.217

binding energy between Mo and B_4N is −6.75 eV, which benefits the fixation of Mo atom. Furthermore, the thermodynamic barrier is 0.61 eV for NRR on Mo-B_4N along the distal pathway, with the potential determining step located in the first protonation process. The superior activity of Mo-B_4N stems from the interaction between the Mo d-band and the N_2 p-band, which effectively weakens the N≡N bond, thereby promoting N_2 activation.

This work demonstrates that Mo-B_4N is a promising single-atom catalyst for N_2-to-NH_3 conversion. Future studies will explore additional factors influencing the NRR performance, such as Mo concentration as well as N_2 coverage, to guide the rational design of efficient catalysts.

Supporting Materials

The supporting materials related to this article can be found at http://doi.org/10.15541/jim20260021. The associated data of this article can be found in Science Data Bank at https://doi.org/10.57760/sciencedb.jim.00043.

References:

[1] LIU K H, ZHONG H X, LI S J, *et al*. Advanced catalysts for sustainable hydrogen generation and storage *via* hydrogen evolution and carbon dioxide/nitrogen reduction reactions. *Progress in Materials Science*, 2018, **92:** 64.

[2] BOULAMANTI A, MOYA J A. Production costs of the chemical industry in the EU and other countries: ammonia, methanol and light olefins. *Renewable and Sustainable Energy Reviews*, 2017, **68:** 1205.

[3] YE T N, PARK S W, LU Y F, *et al*. Vacancy-enabled N_2 activation for ammonia synthesis on an Ni-loaded catalyst. *Nature*, 2020, **583(7816):** 391.

[4] QING G, GHAZFAR R, JACKOWSKI S T, *et al*. Recent advances and challenges of electrocatalytic N_2 reduction to ammonia. *Chemical Reviews*, 2020, **120(12):** 5437.

[5] REN Y W, YU C, TAN X Y, *et al*. Strategies to activate inert nitrogen molecules for efficient ammonia electrosynthesis: current status, challenges, and perspectives. *Energy & Environmental Science*, 2022, **15(7):** 2776.

[6] KWON Y I, KIM S K, KIM Y B, *et al*. Nitric oxide utilization for ammonia production using solid electrolysis cell at atmospheric pressure. *ACS Energy Letters*, 2021, **6(12):** 4165.

[7] WANG J, JANG H, LI G K, *et al*. Efficient electrocatalytic conversion of N_2 to NH_3 on $NiWO_4$ under ambient conditions. *Nanoscale*, 2020, **12(3):** 1478.

[8] PAN Y, ZHANG C, LIU Z, *et al*. Structural regulation with atomic-level precision: from single-atomic site to diatomic and atomic interface catalysis. *Matter*, 2020, **2(1):** 78.

[9] GUO J W, LIU H M, LI D Z, *et al*. A minireview on the synthesis of single atom catalysts. *RSC Advances*, 2022, **12(15):** 9373.

[10] CHEN L, WANG Q, GONG H R, *et al*. Single Mo atom supported on defective BC_2N monolayers as promising electrochemical catalysts for nitrogen reduction reaction. *Applied Surface Science*, 2021, **546:** 149131.

[11] ZHAO M R, SONG B Y, YANG L M. Two-dimensional single-atom catalyst $TM_3(HAB)_2$ monolayers for electrocatalytic dinitrogen reduction using hierarchical high-throughput screening. *ACS Applied Materials & Interfaces*, 2021, **13(22):** 26109.

[12] SHI K, CUI L X, ZHANG M Y, *et al*. DFT study the influence of active site structure on the electrocatalytic nitrogen reduction reaction. *Fuel*, 2025, **380:** 133174.

[13] XU M M, JI Y J, QIN Y Y, *et al*. A universal descriptor for two-dimensional carbon nitride-based single-atom electrocatalysts towards the nitrogen reduction reaction. *Journal of Materials Chemistry A*, 2024, **12(41):** 28046.

[14] LIANG H, WANG J, QIAO Z, *et al*. Machine-learning-assisted design of novel metallic 2D C_3N_3 supported single/double atom catalysts for nitrogen reduction reaction. *Applied Surface Science* 2025, **689:** 162451.

[15] WANG J, ZHANG Z H, LI Y Y, *et al*. Screening of transition-metal single-atom catalysts anchored on covalent–organic frameworks for efficient nitrogen fixation. *ACS Applied Materials & Interfaces*, 2022, **14(1):** 1024.

[16] ZHOU X Y, CHEN X F, SHU C Z, *et al*. Two-dimensional boron-rich monolayer B_xN as high capacity for lithium-ion batteries: a first-principles study. *ACS Applied Materials & Interfaces*, 2021, **13(34):** 41169.

[17] RAHIMI R, SOLIMANNEJAD M. Exploring the adsorption behavior of O-containing VOCs in human breath on a B_2N monolayer using DFT simulations. *Physical Chemistry Chemical Physics*, 2024, **26(39):** 25567.

[18] SREDOJEVIĆ D N, VUKOJE I, TRPKOV Đ, *et al*. A DFT study of CO_2 electroreduction catalyzed by hexagonal boron-nitride nanosheets with vacancy defects. *Physical Chemistry Chemical Physics*, 2024, **26(10):** 8356.

[19] WEI Y H, GAO F, DU J G, *et al*. Hydrogen storage on Li-decorated B_4N: a first-principle calculation insight. *Journal of Physics D: Applied Physics*, 2021, **54(44):** 445501.

[20] DELLEY B. An all-electron numerical method for solving the local density functional for polyatomic molecules. *The Journal of Chemical Physics*, 1990, **92(1):** 508.

[21] DELLEY B. From molecules to solids with the DMol3 approach. *The Journal of Chemical Physics*, 2000, **113(18):** 7756.

[22] PERDEW J, BURKE K, ERNZERHOF M. Generalized gradient approximation made simple. *Physical Review Letters*, 1996, **77(18):** 3865.

[23] GRIMME S, ANTONY J, EHRLICH S, *et al*. A consistent and accurate *ab initio* parametrization of density functional dispersion correction (DFT-D) for the 94 elements H-Pu. *The Journal of Chemical Physics*, 2010, **132(15):** 154104.

[24] TODOROVA T, DELLEY B. Wetting of paracetamol surfaces studied by DMol3-COSMO calculations. *Molecular Simulation*, 2008, **34(10–15):** 1013.

[25] LIM D H, WILCOX J. Mechanisms of the oxygen reduction reaction on defective graphene-supported Pt nanoparticles from first-principles. *The Journal of Physical Chemistry C*, 2012, **116(5):** 3653.

[26] XUE Z, ZHANG X Y, QIN J Q, *et al*. Anchoring Mo on C_9N_4 monolayers as an efficient single atom catalyst for nitrogen fixation. *Journal of Energy Chemistry*, 2021, **57:** 443.

[27] WU K Y, FENG Z Y, LI Z, *et al*. DFT insights into the stability of single-metal-atoms on Mo-based *o*-MXenes driven by the ligand effect. *Physical Chemistry Chemical Physics*, 2026, **28(10):** 6501.

[28] XIAO B B, LIU H Y, YANG L, *et al*. Design of effective graphene with the TM/O moiety for the oxygen electrode reaction. *ACS Applied Energy Materials*, 2020, **3(1):** 260.

[29] WAN Y C, WANG Z J, LI J, *et al*. Mo_2C-MoO_2 heterostructure quantum dots for enhanced electrocatalytic nitrogen reduction to ammonia. *ACS Nano*, 2022, **16(1):** 643.

[30] WU T W, MELANDER M M, HONKALA K. Coadsorption of NRR and HER intermediates determines the performance of Ru-N_4 toward electrocatalytic N_2 reduction. *ACS Catalysis*, 2022, **12(4):** 2505.

[31] GAO L Y, WANG F T, YU M G, *et al*. A novel phosphotungstic acid-supported single metal atom catalyst with high activity and

selectivity for the synthesis of NH_3 from electrochemical N_2 reduction: a DFT prediction. *Journal of Materials Chemistry A*, 2019, **7(34):** 19838.

[32] ANDERSEN S Z, ČOLIĆ V, YANG S, *et al*. A rigorous electrochemical ammonia synthesis protocol with quantitative isotope measurements. *Nature*, 2019, **570(7762):** 504.

[33] CHENG Y M, CHEN W, HE C, *et al*. New insights into the long-range interaction mechanism of nitrogen reduction. *Journal of Energy Chemistry*, 2025, **106:** 842.

[34] JIANG X Y, TAO B R, LI H D. Multistage construction of Gd-doped g-C_3N_4/$Mo_{15}S_{19}$ composites enabled both N_2 activation and multiple electron transfer for an enhanced photocatalytic nitrogen reduction reaction. *Inorganic Chemistry Frontiers*, 2024, **11(24):** 8866.

[35] QIU W B, XIE X Y, QIU J D, *et al*. High-performance artificial nitrogen fixation at ambient conditions using a metal-free electrocatalyst. *Nature Communications*, 2018, **9:** 3485.

[36] LING C Y, NIU X H, LI Q, *et al*. Metal-free single atom catalyst for N_2 fixation driven by visible light. *Journal of the American Chemical Society*, 2018, **140(43):** 14161.

[37] CUI Q Y, QIN G Q, WANG W H, *et al*. Mo-based 2D MOF as a highly efficient electrocatalyst for reduction of N_2 to NH_3: a density functional theory study. *Journal of Materials Chemistry A*, 2019, **7(24):** 14510.

[38] JI S, WANG Z X, ZHAO J X. A boron-interstitial doped C_2N layer as a metal-free electrocatalyst for N_2 fixation: a computational study. *Journal of Materials Chemistry A*, 2019, **7(5):** 2392.

[39] HE T W, MATTA S K, DU A J. Single tungsten atom supported on N-doped graphyne as a high-performance electrocatalyst for nitrogen fixation under ambient conditions. *Physical Chemistry Chemical Physics*, 2019, **21(3):** 1546.

[40] CAO Y Y, DENG S W, FANG Q J, *et al*. Single and double boron atoms doped nanoporous C_2N-h_2D electrocatalysts for highly efficient N_2 reduction reaction: a density functional theory study. *Nanotechnology*, 2019, **30(33):** 335403.

[41] ZHAI X W, LI L, LIU X Y, *et al*. A DFT screening of single transition atoms supported on MoS_2 as highly efficient electrocatalysts for the nitrogen reduction reaction. *Nanoscale*, 2020, **12(18):** 10035.

[42] LIU K, FU J W, ZHU L, *et al*. Single-atom transition metals supported on black phosphorene for electrochemical nitrogen reduction. *Nanoscale*, 2020, **12(8):** 4903.

[43] LI H Y, YANG L, WANG Z X, *et al*. N-heterocyclic carbene as a promising metal-free electrocatalyst with high efficiency for nitrogen reduction to ammonia. *Journal of Energy Chemistry*, 2020, **46:** 78.

钼吸附二维硼氮单层材料催化氮还原反应的密度泛函理论计算

李 智[1], 张俊苗[1], 冯紫阳[1], 肖蓓蓓[1], 宋二红[2]

(1. 江苏科技大学 能源动力学院, 镇江 212003; 2. 中国科学院 上海硅酸盐研究所, 上海 200050)

摘 要: 电催化氮还原反应被视为可持续合成氨的重要路径, 开发高活性、高选择性的催化剂是该技术的核心挑战。本研究通过密度泛函理论计算, 系统探究了钼修饰 B_2N、B_3N 及 B_4N 单层材料的氮还原反应性能。钼与基底间的强相互作用确保了体系稳定性, Mo-B_2N、Mo-B_3N 和 Mo-B_4N 的结合能分别为–8.39、–5.91 和–6.75 eV。研究表明, 钼活性位点能有效活化氮气分子, 吸附后 N≡N 键长由气相中的 1.108 Å 分别延长至 1.128 Å (Mo-B_2N)、1.132 Å (Mo-B_3N)和 1.132 Å (Mo-B_4N)。自由能分析表明, Mo-B_2N、Mo-B_3N 和 Mo-B_4N 的热力学能垒分别为 1.21、1.07 和 0.61 eV, 其中 Mo-B_4N 展现出最优催化活性, 证实配位环境可有效调控钼的反应活性。电子结构分析揭示了 N≡N 键强度与热力学能垒的关联性, N≡N 键越弱, 氮还原反应活性越强。此外, 300 K 室温下的结构刚性保持验证了 Mo-B_4N 优异的热力学稳定性。综上, Mo-B_4N 在电催化氮还原反应中兼具高活性与稳定性。本研究为氮还原电催化剂的设计提供了理论指导, 并提出了具有实验可行性的候选体系。本文数据集可在 https://www.doi.org/10.57760/sciencedb.jim.00043 中访问获取。

关 键 词: 氮还原反应; 密度泛函理论; 单原子催化

中图分类号: TQ174 **文献标志码:** A **文章编号:** 1000-324X(2026)10-1517-08

Supporting Materials

Density Functional Theory Computation of Mo-adsorbed Two-dimensional Boron-nitrogen Monolayers for Nitrogen Reduction Reaction

LI Zhi[1], ZHANG Junmiao[1], FENG Ziyang[1], XIAO Beibei[1], SONG Erhong[2]

(1. School of Energy and Power Engineering, Jiangsu University of Science and Technology, Zhenjiang 212003, China; 2. Shanghai Institute of Ceramics, Chinese Academy of Sciences, Shanghai 200050, China)

S1 Computational method

The adsorption energy (E_{ads}) of intermediate is determined by

$$E_{ads} = E_{system} - E_{catalyst} - E_m \quad (S1)$$

where E_{system}, $E_{catalyst}$ and E_m represent the total energies of the adsorption system, the catalyst and the intermediate, respectively.

The binding energies (E_b) between the Mo atom and its substrate are calculated by

$$E_b = E_{system} - E_{catalyst} \quad (S2)$$

The electrochemical synthesis of NH_3 from N_2 involves a six-step proton-electron transfer process, *i.e.*, $N_2 + 6H^+ + 6e^- \rightarrow 2NH_3$. The Gibbs free energy change (ΔG) of each elemental step is computed based on the computational standard hydrogen electrode (SHE) model proposed by Nørskov *et al.*[S1] wherein the chemical potential of the proton-electron ($H^+ + e^-$) pair equaled to one-half of gaseous H_2 at standard condition. Therefore, the ΔG is given by

$$\Delta G = \Delta E + \Delta ZPE - T\Delta S + \Delta G_U + \Delta G_{pH} \quad (S3)$$

where ΔE is the energy difference, ΔZPE and ΔS represent the changes in zero-point energy and entropy, respectively, derived from vibrational frequency calculations. Herein, the temperature T was set to be 298.15 K. The effect of applied potential U (relative to SHE) is incorporated into the term $\Delta G_U = -eU$ (e is the elementary charge). The effect of proton concentration $[H^+]$ is considered through the term $\Delta G_{pH} = -k_B T \ln[H^+] = pH \times k_B T \ln 10$, wherein pH 0 is used under acidic environment, and k_B represents the Boltzmann constant.

Table S1 Comparison of adsorption energies with and without vdW corrections

Energy	NN	NNH	NNH_2	N	NH	NH_2	NH_3
With corrections/eV	−1.235	−2.925	−3.920	−8.270	−5.318	−4.230	−1.882
Without corrections/eV	−1.139	−2.820	−3.789	−8.232	−5.251	−4.133	−1.779
Difference/eV	−0.096	−0.105	−0.131	−0.038	−0.067	−0.097	−0.103

Table S2 Comparison of ΔG_{max} cited from the previous reports

Catalyst	ΔG_{max}/eV	Ref.
Mo-B_4N	0.61	This work
$Mo_3(HAB)_2$	0.66	[11]
Mo-C_4N_3	0.76	[13]
MoPc-TFPN	0.21	[15]
Mo-C_3N_3	0.41	[14]
Mo-BN	1.01	[12]
Mo-GR	0.71	[12]
Mo-GDY	0.43	[12]
Mo-C_9N_4	0.40	[26]

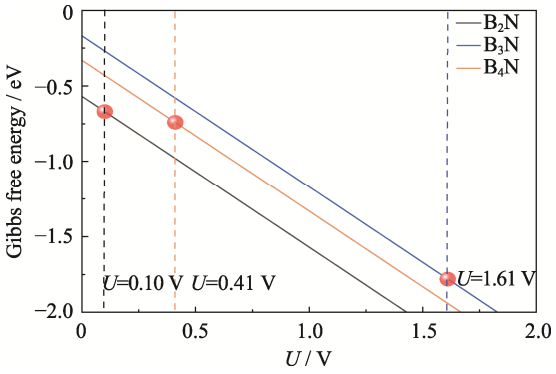


Fig. S1 Free energies of hydrogen adsorption ΔG_H under different potentials

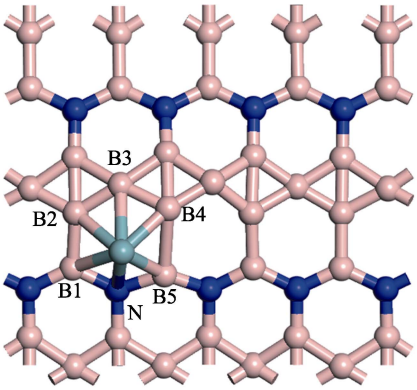


Fig. S2 Labeled coordination environment of Mo-B_4

References:

[S1] NØRSKOV J K, ROSSMEISL J, LOGADOTTIR A, *et al*. Origin of the overpotential for oxygen reduction at a fuel-cell cathode. *The Journal of Physical Chemistry B*, 2004, **108(46):** 17886.